

# Simultaneous Swift X-ray and UV views of comet C/2007 N3 (Lulin)

J.A. Carter<sup>1</sup>, D. Bodewits<sup>2</sup>, A.M. Read<sup>1</sup>, and S. Immler<sup>2,3</sup>

<sup>1</sup> Department of Physics and Astronomy, University of Leicester, Leicester, LE1 1RH, UK  
e-mail: jac48@star.le.ac.uk  
e-mail: amr30@star.le.ac.uk

<sup>2</sup> Department of Astronomy, University of Maryland, College Park, MD 20742-2421, USA  
e-mail: dennis@astro.umd.edu

<sup>3</sup> Astrophysics Science Division, Code 662, NASA Goddard Space Flight Center, Greenbelt, MD 20771, USA  
e-mail: stefan.m.immler@nasa.gov

Received 25 August 2011; Accepted 6 March 2012

## ABSTRACT

**Aims.** We present an analysis of simultaneous X-Ray and UV observations of comet C/2007 N3 (Lulin) taken on three days between January 2009 and March 2009 using the *Swift* observatory.

**Methods.** For our X-ray observations, we used basic transforms to account for the movement of the comet to allow the combination of all available data to produce an exposure-corrected image. We fit a simple model to the extracted spectrum and measured an X-ray flux of  $4.3 \pm 1.3 \times 10^{-13}$  ergs cm<sup>-2</sup> s<sup>-1</sup> in the 0.3 to 1 keV band. In the UV, we acquired large-aperture photometry and used a coma model to derive water production rates given assumptions regarding the distribution of water and its dissociation into OH molecules about the comet's nucleus.

**Results.** We compare and discuss the X-ray and UV morphology of the comet. We show that the peak of the cometary X-ray emission is offset sunward of the UV peak emission, assumed to be the nucleus, by approximately 35,000 km. The offset observed, the shape of X-ray emission and the decrease of the X-ray emission comet-side of the peak, suggested that the comet was indeed collisionally thick to charge exchange, as expected from our measurements of the comet's water production rate ( $6\text{--}8 \times 10^{28}$  mol. s<sup>-1</sup>). The X-ray spectrum is consistent with solar wind charge exchange emission, and the comet most likely interacted with a solar wind depleted of very highly ionised oxygen. We show that the measured X-ray lightcurve can be very well explained by variations in the comet's gas production rates, the observing geometry and variations in the solar wind flux.

**Key words.** Comets: individual: Lulin - X-rays: general - Ultraviolet: general

## 1. Introduction

Comets emit X-rays via the process of solar wind charge exchange (SWCX). Gas in the coma of the comet donates one or more electrons into an excited energy level of a highly-charged ion of the solar wind. In the subsequent relaxation of the ion, a UV or X-ray photon is emitted (Lisse et al. 1996; Cravens 1997; Krasnopolsky 1997).

SWCX in comets probes states of the solar wind throughout the heliosphere (Schwadron & Cravens 2000; Kharchenko & Dalgarno 2001). To date, over 20 comets have been observed in X-rays (Lisse et al. 1996; Dennerl et al. 1997; Lisse et al. 2004; Krasnopolsky 2006; Bodewits et al. 2007).

This sample contains a broad variety of comets, solar wind environments and observational conditions and clearly demonstrates the diagnostics available from cometary charge exchange emission. Several of those comets showed interesting large scale structures in X-ray such as the jets in 2P/Encke (Lisse et al. 2005), the Deep Impact triggered plume in 9P/Tempel 1 (Lisse et al. 2007), and the disintegrating comets 73P/Schwassmann-Wachmann 3 and C/1999 S4 (LINEAR) (Wolk et al. 2009). These interpretations relied on ground-based observations to initially identify those structures. Several attempts have been made to explain the long-term variability of cometary X-ray emission (Lisse et al. 1999; Neugebauer et al. 2000; Lisse et al. 2005; Willingale et al. 2006; Lisse et al. 2007) via relationships between the comet gas production rate,

the heliocentric distance, and the behaviour of the solar wind. This paper however presents the first endeavour to directly constrain the cometary gas production rates and relate this to the observed X-ray variability by employing *Swift*'s co-aligned instrument suite, allowing us to make simultaneous X-ray and UV measurements from a single spacecraft.

C/2007 N3 (Lulin) is a dynamically new comet that was discovered by Lin Chi-Sheng and Ye Quanzhi at Lulin Observatory, Taiwan, in 2007. In this paper we analyse data from comet Lulin obtained by the *Swift* satellite (Gehrels et al. 2004) on several days in early 2009 as part of its Targets of Opportunity programme for non-gamma ray burst targets. The days were chosen to sample emission from the comet at various stages during its passage into and out of the inner solar system, taking advantage of its high activity and its close proximity to Earth. An initial analysis of these observations using data from the *Swift* UV grism was discussed in Bodewits et al. (2011).

Comet Lulin moves in an orbit of low inclination of just  $1.6^\circ$  from the ecliptic, allowing us to link measured solar wind data from the Solar Terrestrial Relations Observatory spacecraft (STEREO, spacecraft A, part of the PLASTIC plasma package, Blush et al. 2005) to our observations. We expected that this comet would sample the low-latitude, highly-charged solar wind and that the intensity of this emission would reflect changes in the solar wind flux, the quantity of neutral species in the comet's atmosphere and the distance to the observer, similar to what has been seen in other near-ecliptic comets (e.g. 2P/Encke (Lisse et al. 1999, 2005); P/Tempel 1 (Lisse et al. 2007)).

The observations were taken around solar minimum, when the solar wind can be simplified to the stratification of a slow, low-latitude wind originating about the solar equator and a higher-latitude, faster wind. The heavy-ion freeze-in temperature at the solar corona determines the ion composition of the out-flowing solar wind. In the bimodal state outside solar maximum, the polar wind has a lower ion freeze-in state than the wind at lower latitudes (Geiss et al. 1995). The nominal low-latitude solar wind flows radially away from the Sun, yet the Sun is rotating, resulting in a Parker spiral outflow (Parker 1958). However, this flow contains streams of plasma with different radial velocities. Co-rotating Interaction Regions (CIRs) occur when a faster stream piles up against the slower, ambient plasma, resulting in an upstream compression region and a downstream rarefaction region. CIRs are characterised by an increase in ion density (with a thickness of  $\sim 0.1$  AU) followed by a decrease in this density, and a corresponding sharp increase in the ion velocity (Gosling & Pizzo 1999, and references therein). They are found at low to mid heliospheric latitudes. Coronal Mass Ejections (CMEs, or ICMEs when they are found within interplanetary space) however, do not form part of the nominal co-rotating solar wind flow, but are large clouds of fast moving plasma ejected from the Sun with distinctive compositional signatures. Along with differences between the fast and slow wind compositional fractionation as described above, transient events such as ICMEs show marked abundance signatures that can be used to identify plasma of this type. The presence of highly-charged iron, elevated oxygen states along with enhanced  $\alpha$ -to-proton ratios for exam-

ple are indicators of ICME plasma (Richardson & Cane 2004; Zurbuchen & Richardson 2006; Zhao et al. 2007).

This paper is organised as follows. In Section 2 we discuss the data analysis steps taken for both the X-ray and UVOT data sets. In Section 3, we discuss our background and spectral analysis of the XRT data along with the X-ray radial extent of the comet, the morphology of the X-ray and UV emission, the gas production rates of the comet and the X-ray temporal variability. We finish with our conclusions in Section 4.

## 2. Data reduction

### 2.1. X-ray telescope

We use data from the X-ray telescope (XRT; Burrows et al. 2005) in photon counting mode. The XRT is sensitive over the energy range 0.2 to 10 keV, has an effective area of  $\sim 80$  cm<sup>2</sup> at 1 keV (Godet et al. 2009), a spectral resolution of  $\sim 130$  eV at Si-K $\alpha$  (Pagani et al. 2011) and a sensitivity limit of  $2 \times 10^{-14}$  ergs cm<sup>-2</sup> s<sup>-1</sup>. The primary source of the XRT particle-induced background is protons incident on the focal plane, swept up as *Swift* moves in its low-Earth orbit.

The 14 *Swift* XRT observations used in this analysis, taken on three different days (2009-01-28, 2009-02-16 and 2009-03-04, 2009 UT) are listed in Table 1. These observations were at fixed pointings and *Swift* did not track the comet. Ephemeris data for the comet were obtained from the Horizons website<sup>1</sup>. We used the cleaned XRT event lists which have been filtered for periods of high background by the standard *Swift* processing chain. The event files had also been adapted for an improvement in the gain function of the XRT (XRT instrument team, private communication). No bright X-ray astronomical point sources were formally detected in the field-of-view (FOV) for any of the pointings by the source detection algorithm *detect* of the HEASARC task XIMAGE<sup>2</sup>.

For every event file we transformed each individually recorded X-ray photon in detector space, using the ephemeris information to account for the comet's movement across the sky. We calculated the change in Right Ascension and Declination of each event and calculated the new detector coordinates accordingly. Every exposure was transformed so that the nominal position of the comet at the exposure start was found at the centre of the detector, and we accounted for the change in Sun-direction by rotating each frame. We then stacked these event files together to improve the signal to noise and adapted the exposure keywords appropriately. Vignetted exposure maps were produced for each observation. Each exposure map was stretched to account for the movement of the comet and shifted and rotated as per the steps applied to the event files. All exposure maps were stacked to provide a combined exposure map to accompany the stacked event file.

We created a smoothed image of the stacked events and divided this by the stacked exposure map to produce an exposure-corrected image. As there was no significant emission detected above 1 keV, we study only photons with  $E < 1$  keV here. We

<sup>1</sup> <http://ssd.jpl.nasa.gov/horizons.cgi>

<sup>2</sup> <http://heasarc.nasa.gov/xanadu/ximage/ximage.html>

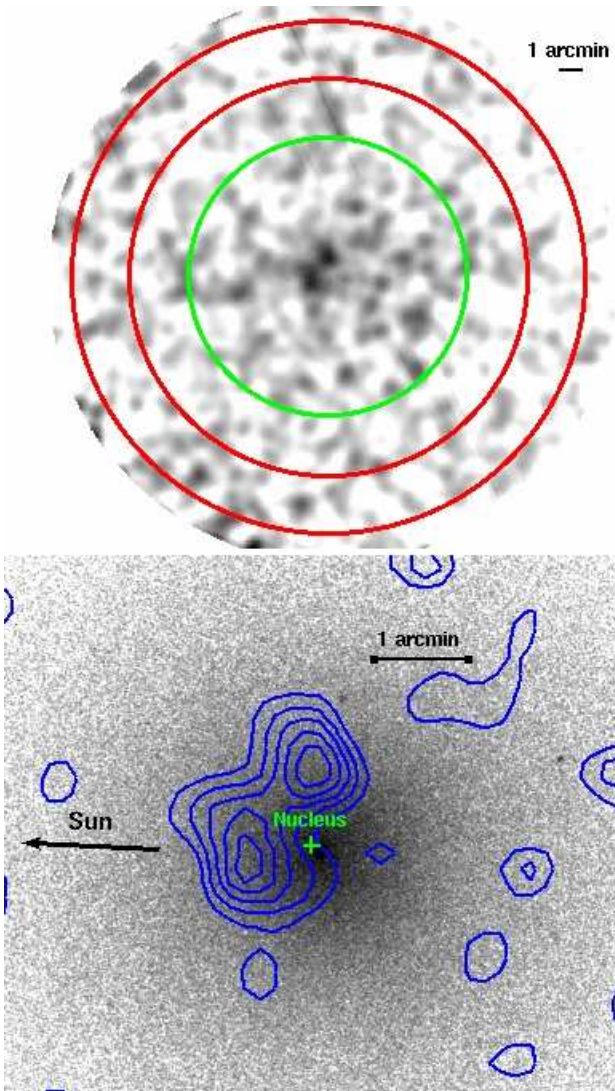


**Fig. 1.** Upper panel: a smoothed 0.3 to 1 keV exposure corrected image of the stacked XRT event list following the transformations described in Section 2.1. The circle (green) and annulus (red) refer to regions used for spectral analysis, see Section 3.1. Lower panel: zoomed-in UV image of the comet, from the first UVW1 exposure of observation 31332 (see Table 1), taken with a pointing Right Ascension and Declination of  $(231.44^\circ$  and  $-17.89^\circ$ ), with X-ray contours from the upper image overlaid. Contours start at  $1.0 \times 10^{-3}$  ct  $s^{-1}$  arcmin $^{-2}$  ( $\sim 6.5$  sigma above the background), and increase in increments of  $0.4 \times 10^{-3}$  ct  $s^{-1}$  arcmin $^{-2}$ . A one arcminute bar is shown on each panel.

restrict the lower limit of our analysis to 0.3 keV due to the uncertain calibration of the XRT below this energy (Godet et al. 2009). A 0.3 to 1 keV exposure-corrected image is shown in Figure 1 (upper panel), which has been rotated so that the Sun vector is as for the first observation of the data set. This image has been smoothed employing a Gaussian filter with FWHM 4.6 pixels (one pixel equals 2.36 arcseconds side length).

## 2.2. UV-Optical telescope

Along with the X-ray observations, the *Swift*-Ultraviolet/Optical Telescope (UVOT; Roming et al. 2005) acquired 75 observations of comet Lulin using its optical and UV broad-band filters. UVOT provides a  $17 \times 17$  arcminute FOV, with a plate scale of 1 arcsecond/pixel and a point spread function of 2.5 arcseconds FWHM (Mason et al. 2004). Additionally, on 2009-01-28 the UV grism was used to acquire low resolution ( $\lambda/\delta\lambda = 100$ ) spectra of the comet (Bodewits et al. 2011). UVOT images of comet Lulin using the uvw1 ( $\lambda_c$  2600Å, FWHM 700Å) and v-band ( $\lambda_c$  5468Å, FWHM 750Å) filters are discussed later in Section 3.2.

Water vapour and its fragment species are the most abundant volatiles in cometary comae. Comet Lulin produced no more than 2-5%  $\text{CO}_2$  and <2% CO (Bodewits et al. 2011; Ootsubo et al. 2010). Given that these molecules have comparable charge exchange cross sections at solar wind ion velocities as  $\text{H}_2\text{O}$  (Mawhorter et al. 2007), the number of water and hydroxyl molecules is a good proxy for the comet's contribution to the variability of the X-ray lightcurve. We used *Swift*'s uvw1 and v-band filters to measure the number of OH molecules in the FOV, and to estimate Lulin's water production rate during our observations.

We measured the comet's flux in large apertures of 400 arcseconds radius to get excellent signal to noise, to sample a large fraction of the coma, and to allow for comparison with the X-ray photometry (Section 3.2). We obtained coma profiles by azimuthally averaging the surface brightness. This was achieved by converting each UVOT image into polar coordinates  $(r, \phi)$  and finding the mean surface brightness at a given radial distance  $(r)$ . By taking the azimuthal-averaged surface brightness for every pixel at a given radial distance  $(r)$  from the optocenter (area of brightest emission, that is not necessarily coincident with the position of the nucleus), we constructed a 2-dimensional azimuthal average image of the comet that was used to search for faint structures.

Although this method assumes the large scale coma to be symmetric, it enables the effective filtering out of stars and other background objects. The coma fills the entire UVOT FOV, but by comparing the signal at the edge of the detector with *Swift* calibration data we estimated a background signal of  $0.005$  counts  $s^{-1}$  pixel $^{-1}$  (uvw1) and  $0.02$  counts  $s^{-1}$  pixel $^{-1}$  (v-band), corresponding to 1% (uvw1) and 13% of the total signal from the comet. At the comet's optocenter, the count rates were high enough to result in some coincidence loss (here approximately 7% for uvw1, and  $\leq 20\%$  for v-band) of the flux in a 5 arcseconds aperture around the optocenter (Poole et al. 2008). We decided not to correct our photometry for this coincidence loss, as it only affected a small fraction of the total flux in the 400 arcsecond aperture. Based on these considerations we estimate stochastic errors to be 5% (uvw1) and 15% (v-band). Absolute errors in the photometry are better than 3% (Breeveld et al. 2011).

The measured fluxes in the filters relevant to this study (uvw1 and v-band) are summarised in Table 1. Note that two UVOT exposures with the same observation ID (31332) were obtained in the same *Swift* orbit, while in observations 31336

**Table 1.** *Swift* XRT and UVOT observations of comet Lulin performed in early 2009, listed by the observation identifier (OBS\_ID). Start and stop times are given for the XRT exposures in the format MM-DD. We also note the XRT livetimes (T), the Sun-comet distance ( $r_h$ ), the Earth-comet distance ( $\Delta$ ), the Sun-Earth-comet (S-E-C) angle and the rate of change in Right Ascension and Declination ( $\Delta$ RA,  $\Delta$ Dec). The horizontal lines separate the three observing periods. We list the UVOT measured fluxes for the uvw1 and v-band filters in 400 arcsecond apertures (see Sec. 2.2). Flux (OH) is the flux in the uvw1 filter after removal for the continuum contribution (see Section 3.3). N(OH) is the number of OH molecules in a 400 arcsecond aperture and Q(OH) is the production rate of OH molecules (see Section 3.3.1). No v-band observations were obtained on 2009-01-28, and we list upper limits for the OH production rates based on the total measured uvw1 flux. Only stochastic errors are given. The systematic uncertainty in the UVOT measured fluxes is less than 5%, and approximately 25% for Q(OH). We list the total number of X-ray photons for each pointing ( $N_x$ ) within the spectral extraction region and between 0.3 and 1 keV, as described in Section 3.1. We also list the measured XRT X-ray fluxes (between 0.3 and 1 keV in cgs units ( $\text{ergs cm}^{-2} \text{s}^{-1}$ ), see Section 3.3.3) in the last column, or upper limits where appropriate (assuming a negligible background).

| OBS_ID             | Start    | Stop     | T<br>(s) | $r_h$<br>(AU) | $\Delta$<br>(AU) | S-E-C<br>(deg) | $\Delta$ RA.<br>(sec/s) | $\Delta$ Dec.<br>(sec/s) | Flux uvw1<br>( $\text{W m}^{-2} \text{sr}^{-1}$ ) | Flux v-band<br>( $\text{W m}^{-2} \text{sr}^{-1}$ ) | Flux (OH)<br>( $\text{W m}^{-2} \text{sr}^{-1}$ ) | N(OH)<br>(molec.)<br>( $\times 10^{33}$ ) | Q (OH)<br>(molec. $\text{s}^{-1}$ )<br>( $\times 10^{28}$ ) | $N_x$ | XRT flux<br>cgs<br>( $\times 10^{-13}$ ) |
|--------------------|----------|----------|----------|---------------|------------------|----------------|-------------------------|--------------------------|---|---|---|---|---|-------|--|
| 31332              | 01-28.00 | 01-28.08 | 2335     | 1.245         | 1.083            | 74.43          | -0.025                  | 0.006                    | $0.30 \pm 0.01$                                   | ...   | ...   | <11.0                                     | <9.65   | 273   | $10.4 \pm 3$                             |
| 31332 <sup>a</sup> |          |          |          |               |                  |                |                         |                          | $0.29 \pm 0.01$                                   | ...   | ...   | <11.0                                     | <9.63   |       | ...                                      |
| 31336              | 01-28.13 | 01-28.14 | 1136     | 1.246         | 1.079            | 74.64          | -0.026                  | 0.006                    | ...   | ...   | ...   | ...                                       | ...   | 138   | <25                                      |
| 31337              | 01-28.19 | 01-28.27 | 2276     | 1.246         | 1.077            | 74.75          | -0.026                  | 0.006                    | ...   | ...   | ...   | ...                                       | ...   | 299   | $11.0 \pm 3$                             |
| 31347              | 02-16.53 | 02-16.55 | 943      | 1.338         | 0.508            | 125.04         | -0.132                  | 0.051                    | $0.59 \pm 0.03$                                   | $0.81 \pm 0.12$                                     | $0.47 \pm 0.06$                                   | $3.16 \pm 0.4$                            | $5.5 \pm 0.7$   | 58    | <6.1                                     |
| 31348              | 02-16.61 | 02-16.62 | 932      | 1.339         | 0.506            | 125.36         | -0.133                  | 0.051                    | $0.60 \pm 0.03$                                   | $0.86 \pm 0.13$                                     | $0.47 \pm 0.06$                                   | $3.11 \pm 0.4$                            | $5.5 \pm 0.6$   | 44    | <6.2                                     |
| 31349              | 02-16.67 | 02-16.69 | 948      | 1.339         | 0.505            | 125.66         | -0.134                  | 0.052                    | $0.60 \pm 0.03$                                   | $0.85 \pm 0.13$                                     | $0.47 \pm 0.06$                                   | $3.11 \pm 0.4$                            | $5.5 \pm 0.6$   | 52    | <6.5                                     |
| 31350              | 02-16.74 | 02-16.75 | 935      | 1.340         | 0.503            | 125.95         | -0.134                  | 0.052                    | $0.60 \pm 0.03$                                   | $0.85 \pm 0.13$                                     | $0.47 \pm 0.06$                                   | $3.11 \pm 0.4$                            | $5.5 \pm 0.7$   | 53    | <5.8                                     |
| 31351              | 02-16.81 | 02-16.82 | 937      | 1.340         | 0.502            | 126.25         | -0.135                  | 0.052                    | $0.60 \pm 0.03$                                   | $0.84 \pm 0.13$                                     | $0.47 \pm 0.06$                                   | $3.10 \pm 0.4$                            | $5.5 \pm 0.7$   | 69    | <9.8                                     |
| 31352              | 02-16.88 | 02-16.89 | 940      | 1.341         | 0.500            | 126.56         | -0.136                  | 0.053                    | $0.59 \pm 0.03$                                   | $0.86 \pm 0.13$                                     | $0.46 \pm 0.06$                                   | $3.04 \pm 0.4$                            | $5.5 \pm 0.6$   | 82    | <10.2                                    |
| 31353              | 02-16.94 | 02-16.95 | 932      | 1.341         | 0.499            | 126.86         | -0.137                  | 0.053                    | $0.60 \pm 0.03$                                   | $0.86 \pm 0.13$                                     | $0.47 \pm 0.06$                                   | $3.05 \pm 0.4$                            | $5.5 \pm 0.6$   | 87    | $7.1 \pm 3$                              |
| 31364              | 03-04.31 | 03-04.33 | 1643     | 1.455         | 0.519            | 149.02         | -0.131                  | 0.037                    | $0.53 \pm 0.03$                                   | $0.60 \pm 0.10$                                     | $0.43 \pm 0.04$                                   | $2.57 \pm 0.3$                            | $4.2 \pm 0.5$   | 84    | <4.2                                     |
| 31365              | 03-04.38 | 03-04.40 | 1653     | 1.456         | 0.520            | 148.74         | -0.130                  | 0.036                    | $0.52 \pm 0.03$                                   | $0.60 \pm 0.10$                                     | $0.43 \pm 0.04$                                   | $2.56 \pm 0.3$                            | $4.2 \pm 0.5$   | 99    | <4.0                                     |
| 31366              | 03-04.44 | 03-04.46 | 1643     | 1.456         | 0.522            | 148.46         | -0.130                  | 0.036                    | $0.52 \pm 0.03$                                   | $0.59 \pm 0.10$                                     | $0.43 \pm 0.04$                                   | $2.59 \pm 0.3$                            | $4.2 \pm 0.5$   | 115   | <6.0                                     |
| 31367              | 03-04.51 | 03-04.53 | 1620     | 1.456         | 0.523            | 148.18         | -0.128                  | 0.035                    | $0.52 \pm 0.03$                                   | $0.59 \pm 0.10$                                     | $0.43 \pm 0.04$                                   | $2.58 \pm 0.3$                            | $4.2 \pm 0.5$   | 108   | <5.8                                     |

<sup>a</sup> Two uvw1 exposures were obtained for the observation 31332.

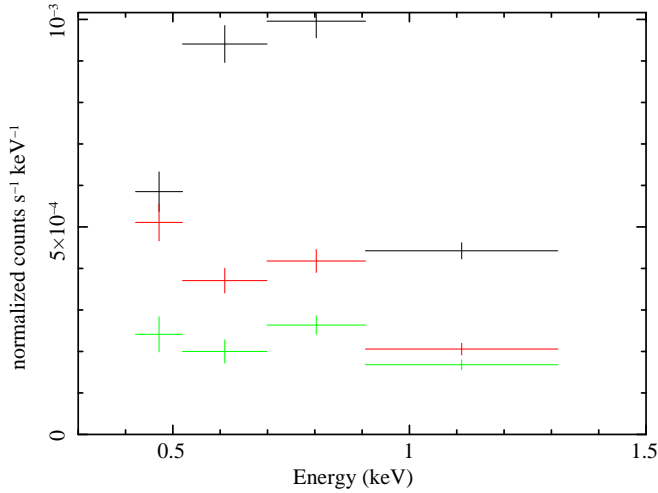


**Fig. 2.** RASS backgrounds for the three sky positions of the comet (see text and Table 1), for 2009-01-28 (black), 2009-02-16 (red) and 2009-03-04 (green).

and 31337 no exposures with the uvw1 or v-band filters were obtained.

### 3. Discussion

#### 3.1. Background and spectral analysis of the XRT data

Comets are extended sources, often larger than the FOV of the observing instrumentation. Additionally, the X-ray background can show considerable temporal and spatial variation. The background subtraction is therefore non-trivial, and we compare two different approaches here. First, we downloaded three ROSAT all-sky survey spectra (radius 1 degree) and the ROSAT PSPCC response matrix from the HEASARC background tool<sup>3</sup>, where any known so-called Long Term Enhancements, due to time-variable SWCX (from exospheric or heliosphere emission, e.g. Collier et al. 2005 or Koutroumpa et al. 2006) have been removed (Snowden et al. 1995). The three pointings were chosen to reflect the comet’s position on the sky during the three observing periods (see Table 1). We plot the three background spectra (from OBS\_IDs 4973969, 4917081, 4814705) in Figure 2. The spectra show a considerable amount of variation. It was decided however, that creating three separate spectra for the comet would be infeasible due to the poor statistics that would be obtained.

The second method, which we deemed more reliable, concentrates instead on a spectrum obtained from the combined spectrum from all the available data for the comet. We show a radial profile of the exposure corrected image in Figure 3. Distances are quoted in arcseconds from the centre of the detector (which, following the procedure described in Section 2.1 is the centre of the comet according to the ephemeris transformations that we had applied to the X-ray data). The radial profile allowed us to constrain the area in the detector plane that we considered to contain emission from the comet by selecting a radius at which the profile drops to the apparent back-

ground level. The peak of the radial profile is offset from the origin of the distance axis. This offset is described in more detail in Section 3.2.2. We extracted a background spectrum from the stacked event file, using a centrally positioned annulus with inner and outer radii of 500 and 645 arcseconds. We then extracted a spectrum using a centrally positioned circular extraction region, with a radius of 349 arcseconds chosen to maximise the signal to noise. Both regions are shown overlaid on the exposure-corrected image of the stacked events of Figure 1 (upper panel). We applied the appropriate instrument XRT response matrix and effective area correction file (photon counting mode).

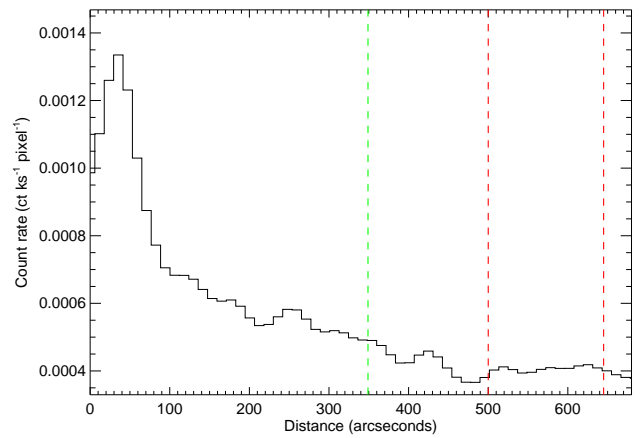


**Fig. 3.** Radial profile of the 0.3 to 1 keV combined XRT exposure-corrected image. The dashed vertical lines indicate the radius of the spectral (green) and the boundaries of the background extraction regions (red), chosen to maximise the signal to noise and to avoid subtracting signal coming from the comet.

The SWCX emission process is characterised by line emission in the soft X-ray band. Using the XSPEC<sup>4</sup> spectral fitting package we fit an un-absorbed SWCX-like simple model to the background-corrected spectrum (shown in Figure 4), incorporating three zero-width Gaussian lines, letting the energies and the line normalisations vary. The lines were found at 0.38 keV, 0.52 keV and 0.64 keV, which we attribute to a blend of helium- and hydrogen-like carbon and nitrogen lines, nitrogen and oxygen lines, and oxygen respectively. The reduced-Cash statistic (maximum likelihood-based statistic for Poisson data, Cash 1979) was 1.3 for 63 degrees of freedom with a not unreasonable goodness of fit of 35%. The goodness of fit should be approximately 50% had the observed spectrum been produced by the model. The un-absorbed flux between 0.3 and 1 keV was found to be  $4.3 \pm 1.3 \times 10^{-13}$  ergs cm<sup>-2</sup> s<sup>-1</sup> (95% confidence). We also note the background-subtracted count rates in two energy bands of interest:  $4.1 \pm 1.1 \times 10^{-3}$  ct s<sup>-1</sup> (0.3 to 0.5 keV) and  $4.1 \pm 1.6 \times 10^{-3}$  ct s<sup>-1</sup> (0.5 to 0.7 keV). We look into the variation of flux with respect to time in Section 3.3.3, in com-

<sup>3</sup> <http://heasarc.gsfc.nasa.gov/cgi-bin/Tools/xraybg/xraybg.pl>

<sup>4</sup> <http://heasarc.gsfc.nasa.gov/docs/xanadu/xspec/index.html>

parison to the behaviour of the solar wind at the time of the observations.

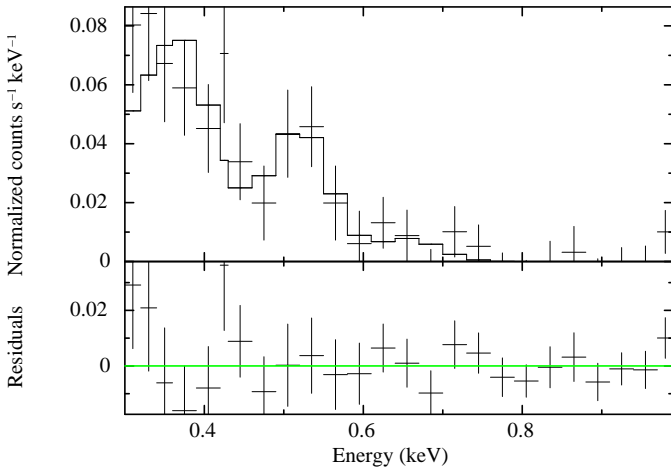


**Fig. 4.** Upper panel: background subtracted spectrum from the combined comet Lulin XRT data set. The model fitted to the data, consisting of three zero-width Gaussian lines as described in the text, is shown by the solid line. Lower panel: residuals to the model fit.

Several sophisticated methods have been developed to analyse cometary SWCX spectra (Beiersdorfer et al. 2003; Kharchenko et al. 2003; Krasnopolsky 2006; Bodewits et al. 2007). We chose to apply a much simpler model here due to the low-quality spectrum achieved, even after stacking of the entire data set to improve the signal to noise. We do not observe any emission above  $\sim 0.8$  keV, in contrast to comets within the *Chandra* survey (Bodewits et al. 2007), which consistently required higher-order transitions of O VIII plus two Ne lines at 0.90 keV (Ne IX) and 1.024 keV (Ne X). The *Swift* XRT has an effective area of  $\sim 65$  cm<sup>2</sup> at  $\sim 0.8$  keV, much lower than the  $\sim 300$  cm<sup>2</sup> at the same energy of the *Chandra* ACIS S3 chip used in the Bodewits et al. (2007) survey. However, the *Swift* XRT effective area increases to a maximum of  $\sim 120$  cm<sup>2</sup> at about  $\sim 1.5$  keV (compared to  $\sim 700$  cm<sup>2</sup> for the *Chandra* ACIS S3 chip), implying that the lack of emission above this energy is due to incoming solar wind compositional effects, which we discuss more in Section 3.3.3. Although the poor signal-to-noise ratio inhibits interpretation of the signal at higher energies, the lack of such a signal may suggest that the comet interacted with a solar wind with a charge state distribution reflecting a very low freeze-in temperature. The spectral shape of the model applied here most closely resembles that of comets 2P/Encke (Lisse et al. 2005) and 73P/Schwassmann-Wachmann 3 (Wolk et al. 2009) of the *Chandra* sample, which sampled the coolest wind of that survey. We comment in more detail about the composition of the interacting solar wind in Section 3.3.3.

## 3.2. Morphology: UV and X-ray

### 3.2.1. Coma and tails

UVOT images for every observing day are shown in Figure 5. The left most column shows the comet in the uvw1 band for each observing periods (panels A, C and F). In this band the comet appears very symmetric around the nucleus, confirming that most of the emission seen in the uvw1 band comes from OH molecules (Section 3.3.1). The comet’s morphology in the v-band is driven by the changing viewing geometry. No v-band observations were obtained on 2009-01-28. On 2009-02-16 the dust coma is elongated in the solar direction. Subtracting the azimuthal profile as determined by the method described in Section 2.2 (c.f. Schleicher & Farnham 2004) reveals both the dust tail (westward) and the anti-tail (eastward); the latter consists of long lived dust emitted near perihelion (panel E). Lulin moves in a retrograde orbit and Earth crossed the comet-Sun plane around 2009-02-26. On 2009-03-04, the observing geometry therefore no longer allows easy separation of particles along different trajectories, resulting in a dust tail in the anti-solar direction (shown by the elongated contours in panel G).

On 2009-01-28, a well defined, narrow tail can be seen to extend westwards (best seen in panel B, where the image is divided by the azimuthal profile). It is not visible in the 2009-02-16 images (panel E). The nature of this narrow tail was first discussed in Bodewits et al. (2011). In this paper it was argued that from the geometry the narrow tail could be either the dust tail or the ion tail (both clearly visible in wide field amateur images obtained in this period), but that while the uvw1 filter has a significant red-leak, it is not very sensitive to the emission usually associated with the blue CO<sup>+</sup> comet tail system (4000 – 5000 Å). It was concluded that it was more likely that the narrow feature arose from continuum emission from dust or ice. No asymmetric feature, however, is visible in the uvw1 and v-band azimuthal profile-subtracted images on 2009-02-16.

As we argued above, the UV filter transmission means that the narrow tail is likely to be small-grained dust rather than ions. The geometric conditions and the fact that the tail was detected in the UV observations in January but not in February suggests that it is the result of enhanced activity of these grains around perihelion. The dust, released around perihelion and pushed away from the Sun, was projected to the west in January, matching the direction of the observed tail. By the time of the February observations, the Earth had moved to the point that we were looking almost straight down this tail. Unfortunately, the lack of UVOT v-band observations preclude the comparison of larger dust grains between the two dates.

### 3.2.2. Solar wind interaction in X-rays

As discussed in the previous section, the OH distribution in the coma was very symmetric and homogeneous during our observations. Past modelling has indeed indicated a transition between thick and thin regimes between  $10^{28}$  and  $10^{29}$  mol. s<sup>-1</sup>. Lulin’s large gas production rate ( $6\text{--}8 \times 10^{28}$  mol. s<sup>-1</sup>, Sec. 3.3.1) made it collisionally thick to charge exchange by solar wind ions (c.f. Lisse et al. 2005 and

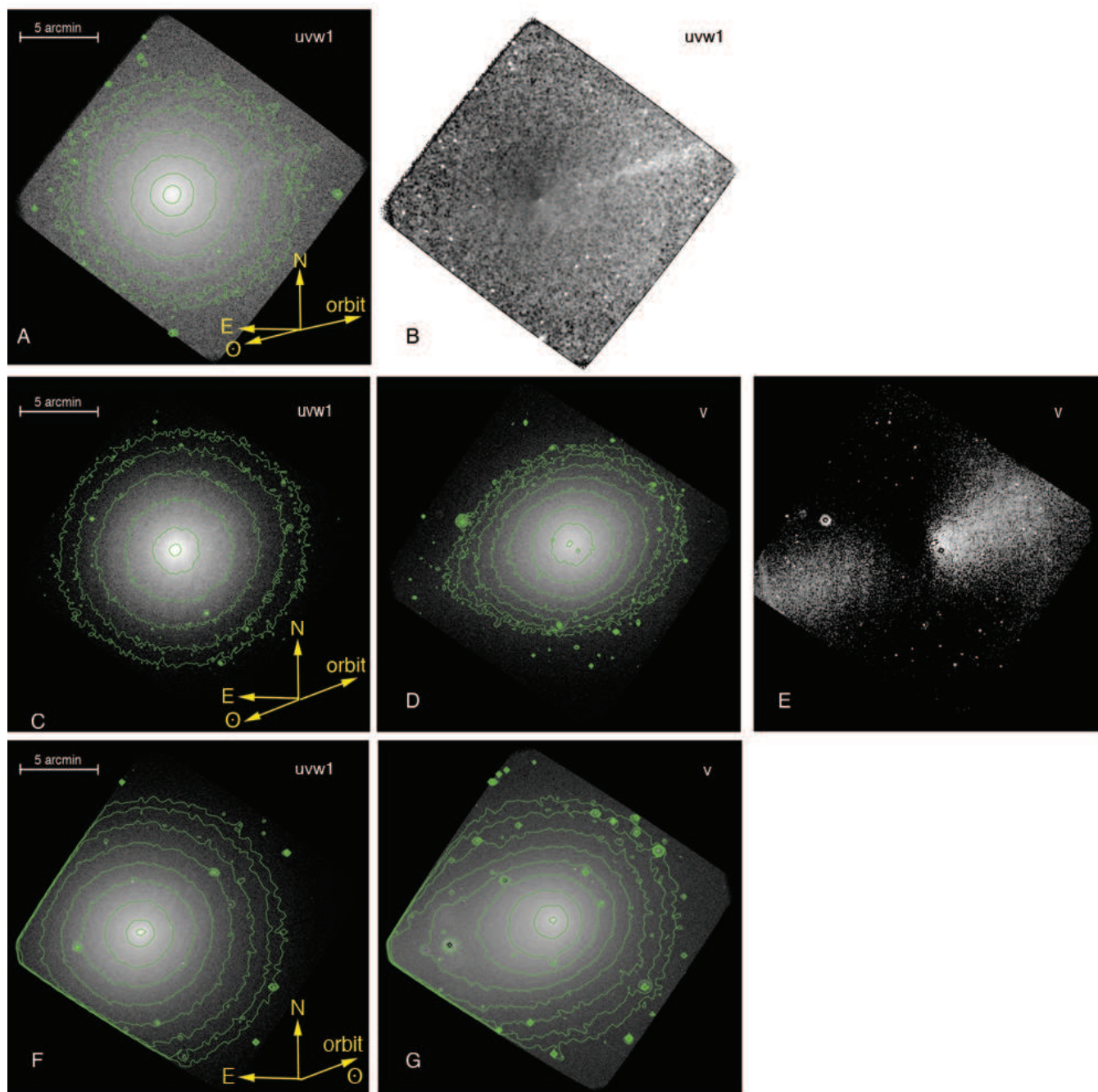


**Fig. 5.** UVOT observations of Comet Lulin. **A.** 2009-01-28, uvw1. **B:** image A divided by coma profile. **C:** 2009-02-16, uvw1. **D:** 2009-02-16, v-band. **E:** image D with the coma profile subtracted. **F:** 2009-03-04, uvw1 **G:** 2009-03-04, v-band. All images are oriented in the same way (east left, north up) and have the same angular scale (UVOT's FOV is  $17 \times 17$  arcminute). Iso-intensity contours are shown on a logarithmic scale to enhance fainter features. In panel **F** the solar direction vector and the orbital vector are coincident.

Bodewits et al. 2007). It is therefore to be expected that when viewed via X-ray emission, the comet would appear as a crescent when observed at phase angles of around 90 degrees, with a significant sunward offset between the maximum of the observed X-ray emission and the nucleus of the comet (cf. Hyakutake (Lisse et al. 1996); Linear S4, (Lisse et al. 2001); C/2001 WM1 (Wegmann & Dennerl 2005)). From the models by Bodewits et al. 2007, most charge exchange reactions in the

coma of a comet with a gas production rate of  $\sim 10^{29}$  mol.  $s^{-1}$  would occur  $10^3 - 10^4$  km from the nucleus (at a distance of 1 AU from the Sun).

In Figure 1 (lower panel) we plot X-ray contours over a UVOT UV image of the comet (from the first observation, 31332 using filter uvw1). As this X-ray image is constructed from images taken at different Sun-Earth-comet angles and geocentric distances (resulting in differing angular extents of

the expected X-ray emission), caution should be exercised when interpreting the implied morphology. A very rough crescent shape can be seen in Figure 1 (lower panel). Assuming the exposure-weighted distance of 0.685 AU to the comet we find that the X-ray maximum is offset in the sunward direction from the UV maximum by  $\sim 35,000$  km (foreshortened by the observing geometry). While in line with other comet observations (Wegmann & Dennerl 2005; Dennerl et al. 2003), this stand off distance is greater than expected by the model results of Bodewits et al. (2007), who predict the brightness peak around 10,000 km for  $Q = 10^{29}$  molecules/s at a heliocentric distance 1 AU, and less than predicted by the model of Wegmann et al. (2004), who predict 66,000 km under the same circumstances.

### 3.3. Temporal variations

Variations in the comet's X-ray luminosity are driven by variations in the comet's gas production rate, in the solar wind ion flux, and by the solar wind ion content. Along with its X-ray observations, *Swift* simultaneously obtained UV/optical observations of the comet, which provide a measure of the comet's gaseous activity. The solar wind is currently sampled by various spacecraft and data from these spacecraft are the best proxies for near-Earth comet environments. In this section we interpret our observations in terms of the variability of both the cometary neutral gas content and the solar wind ion flux.

#### 3.3.1. Gas production rates

At the wavelengths covered by UVOT, comets are seen in sunlight reflected by cometary dust, with several bright molecular emission bands superposed. The uvw1 filter is well placed to observe the three very strong OH vibrational transitions between 280 and 312 nm. Lulin's spectrum was only slightly reddened ( $< 10\%$  per 1000 Å; Bodewits et al. 2011; Lin et al. 2007). We therefore assumed an un-reddened solar continuum, and convolved this with the uvw1 and v-band filter transmissions to determine how much the continuum contributes to the uvw1 flux. If we further assume that the flux in the v-band filter is dominated by continuum emission (while in truth it is contaminated by the fluorescent emission of various molecules, predominantly  $C_2$  and  $NH_2$ ). The OH flux is then given by **Equation 1**:

$$F_{OH} = F_{uvw1} - (0.15 \times F_V) \quad (1)$$

where  $F_{uvw1}$  and  $F_V$  are the fluxes measured in the uvw1 and v-band filters. The factor 0.15 originates from the ratio  $F_{uvw1}/F_V$  for a solar spectrum. From Table 1, on 2009-02-16 the continuum contribution (here assumed to be any contributions other than from OH) to the flux measured in the uvw1 band was approximately 21%; on 2009-03-04 it was 17%. We consider the possibility that there is a non-negligible contribution from the fluorescence emission of  $C_2$  to the v-band measured flux. Using the total  $C_2$  flux within this band determined from our work with the *Swift* grism (Bodewits et al. 2011), we estimate the contribution to be  $0.25 \text{ W m}^{-2} \text{ sr}^{-1}$ . This corresponds to an

over-subtraction of 8% in the calculation of the OH flux using Equation 1. As this is well within the errors quoted in Table 1, we consider this contamination of marginal consequence.

Using the molecules' fluorescent rate (Schleicher & A'Hearn 1988), the number of OH molecules in the aperture can be derived (Feldman et al. 2005). The results are listed in Table 1. To derive production rates, we modelled the OH and water distribution, and compared this with the measured OH number densities. This model is based on the Haser model (Haser 1957; Festou 1981) and is discussed in greater detail in Bodewits et al. (2011).

The use of broad band filters implies that our results are a relatively crude estimate of the comet's water production and we estimate the systematic error to be around 25%. The resulting OH production rates are summarised in Table 1. No v-band observations were obtained on 2009-01-28, and without accounting for the continuum removal we find a 3-sigma upper limit of  $Q_{OH} < 1 \times 10^{29} \text{ mol. s}^{-1}$ , in good agreement with the production rates of  $5.8 \pm 0.6$  (1-sigma) to  $6.9 \pm 0.6 \times 10^{28} \text{ mol. s}^{-1}$  measured with the grism (Bodewits et al. 2011). On 2009-02-16 and 2009-03-04 the OH production rates were  $5.5 \pm 1.0 \times 10^{28} \text{ mol. s}^{-1}$  and  $4.2 \pm 1.0 \times 10^{28} \text{ mol. s}^{-1}$ , respectively.

The OH production rates were converted to water production rates assuming a branching ratio for the formation of OH from  $H_2O$  of 85% (Huebner et al. 1992; Combi et al. 2004). In Figure 6 we show these rates versus time, for this work and other measurements (Combi et al. 2009; Bonev et al. 2009; Ootsubo et al. 2010; Bodewits et al. 2011, and D. Schleicher (private communication)). Our measurements indicate that the comet's activity was slowly decreasing after it had reached perihelion on UT Jan. 10.64, 2009, in good agreement with other measurements.

Several studies found that gas production rates varied on a day-to-day basis by as much as 50%, suggesting strong diurnal effects on the comet (Bodewits et al. 2011; Combi et al. 2009; Knight & Schleicher 2009). Based on the phasing of CN jets, Knight & Schleicher (2009) found a rotation period for comet Lulin of  $42 \pm 0.5$  hr. Even though our UVOT broadband observations on 2009-02-16 and 2009-03-04 sampled the comet every hour for about half a day and thus we did not observe the comet for a full rotation period, our data showed no significant short term flux variations.

To estimate the comet's neutral gas contribution to its X-ray variability one needs to know the number of neutral coma molecules in the FOV. It can be assumed that the X-rays are mostly driven by SWCX with  $H_2O$  and OH (Bodewits et al. 2006). We therefore need to know the sum of the number of  $H_2O$  and OH molecules in the aperture. If the aperture were large enough, the total number of OH molecules would be 0.85 times the number of  $H_2O$  molecules (the branching ratio of the  $H_2O$  to OH photodissociation process), and the total number of neutral molecules in the FOV would thus be 2.2 times the number of OH molecules present. However, in apertures smaller or equivalent to the Haser scale-lengths for  $H_2O$  to OH dissociation (of the order of  $10^5$  km at 1 AU from the Sun), the number of  $H_2O$  molecules will be larger than the number of OH molecules. For the apertures used here ( $\sim 3.1 \times 10^5$  km,

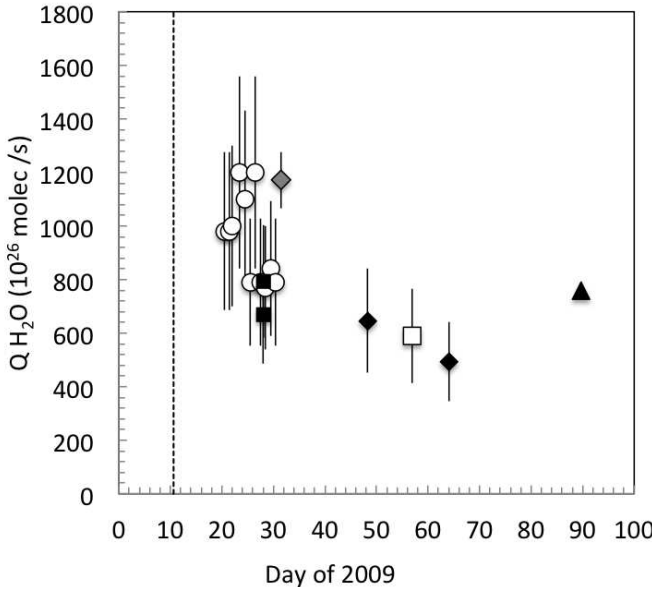


**Fig. 6.** Gas production rates of  $\text{H}_2\text{O}$  vs time, calculated for our observing periods on 2009-02-16 and 2009-03-04 (solid, black diamonds). We also plot  $\text{H}_2\text{O}$  production rates from Combi et al. 2009 (circles), Schleicher 2009 (private communication, open squares), Bodewits et al. 2011 (filled squares), Ootsubo et al. 2010 (filled triangle) and Bonev et al. 2009 (solid, grey diamond). The dashed vertical line indicates the date of the perihelion passage of the comet.

$\sim 1.45 \times 10^5$  km and  $\sim 1.51 \times 10^5$  km radius, for the three observing periods), the total number of  $\text{H}_2\text{O}$  plus OH molecules, calculated by Haser modelling, are 1.54, 1.56, and 1.57 times the number of observed OH molecules on 2009-01-28, 2009-02-16, and 2009-03-04, respectively. This factor incorporates the lifetimes of the  $\text{H}_2\text{O}$  and OH molecules with cometary distance from the Sun and accounts for the proportion of  $\text{H}_2\text{O}$  compared to OH observed depending on aperture size. For the 2009-01-28 measurement the aperture is much larger than the Haser scale length, whereas the factors for 2009-02-16 and 2009-03-04 are adjusted to account for the smaller apertures used.

To estimate the number of water and OH molecules on 2009-01-28, when we did not have any v-band images to subtract the continuum emission from the uvw1 filter, we used the OH production rates derived from the grism observations and used our Haser model to estimate the number of molecules in a 400 arcseconds radius aperture.

### 3.3.2. Solar wind

We took data from STEREO A to investigate the behaviour of the solar wind in early 2009, shown in Figure 7. We plot the solar wind proton speed and flux, mapped to the approximate location of the comet. STEREO A is found ahead of the Earth in its orbit on the ecliptic plane. In order to map the solar wind from STEREO A to the position of the comet at the three observing periods, we used the time shift procedure described by Lisse et al. (1999) and Neugebauer et al. (2000). The cal-

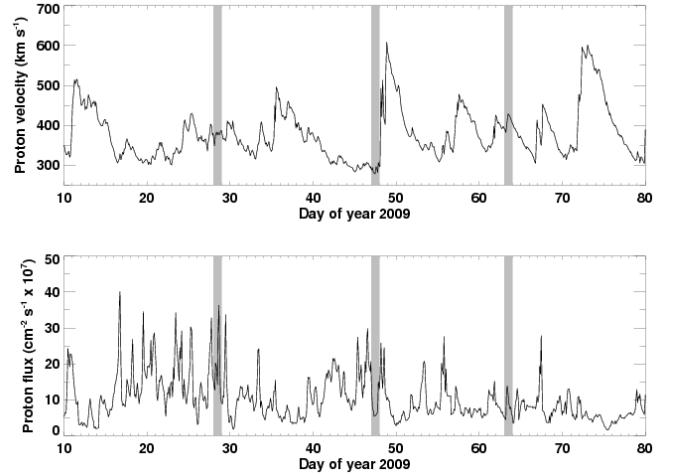


**Fig. 7.** Solar wind parameters, taken from STEREO A, that have been co-rotationally mapped to the location of the comet. Upper panel: proton velocity. Bottom panel: proton flux. The three observing periods are highlighted within the light-grey shaded areas.

culations are based on the comet ephemeris, the location of the comet and STEREO A, and the bulk solar wind velocity measured by STEREO A. With this procedure, the time delay between an element of the co-rotating solar wind arriving at the proton monitor and the comet can be predicted. Although this mapping is an approximation that does not take propagating shocks or latitudinal structures in the wind into account (Neugebauer et al. 2000; Bodewits et al. 2007), the relatively close proximity of the comet and its low heliocentric latitude ( $<1$  degree during our observations) aid its reliability.

On 2009-01-28, there is a delay of 2.5 days between the solar wind measured by STEREO A and the solar wind arrival at the comet, mostly due to the longitudinal difference. On 2009-02-16, this delay is 0.8 days, and on 2009-03-04 the comet leads STEREO A by 1.8 days. It is of note that the uncertainty in the solar wind arrival time is the largest in January, when the comet was still at 1 AU from Earth versus 0.5 AU in March.

The averaged solar wind proton fluxes, were 15, 5 and  $14 \times 10^7 \text{ cm}^{-2} \text{ s}^{-1}$  for 2009-01-28, 2009-02-16, and 2009-03-04 respectively. The average solar wind proton speeds for the three observing periods were  $\sim 370$ , 280 and  $420 \text{ km s}^{-1}$ , implying solar wind densities of 4.2, 1.9 and  $3.4 \text{ cm}^{-3}$ . Inspection of long term solar wind data indicate the presence of several CIRs (a compression region followed by a rarefaction, as described in Section 1) during the early part of 2009. The most notably of these occurred just after the second observing period, as indicated by sharp increases in solar wind proton velocity. In addition a weaker CIR occurred during the third observing period, shown in the upper panel of Figure 7. The low solar wind proton densities may be explained by the presence of these CIRs. The solar wind data further show that a CIR reached the comet around 2009-02-05 (day of year 36). Considering the uncertainty in the time delay of our propagation model, we consider it likely that it was this CIR that caused a disconnection event at the comet, reported by Shi et al. 2011.

### 3.3.3. X-ray lightcurve

In Figure 8 (upper panel) we plot the background-corrected XRT fluxes in the energy band 0.3 to 1 keV for each observation (accounting for the areas of the spectral extraction regions to convert to the stated flux units), or the upper limit where appropriate. We also show the predicted X-ray flux, calculated from the product of solar wind proton flux and the number of neutral molecules in the FOV, corrected for the Earth-comet distance (Equation 2):

$$F_x = k * \frac{N_{\text{gas}} * F_{\text{sw}}(r_h)}{\Delta^2} \quad (2)$$

where  $k$  is a normalisation constant,  $N_{\text{gas}}$  is the total number of water group molecules available to contribute to the charge exchange process derived from our UVOT observations (see Section 3.3.1),  $F_{\text{sw}}(r_h)$  are the solar wind proton fluxes at the comet (as described in Section 3.3.2), and  $\Delta$  are the Earth-comet distances (as listed in Table 1). We normalised to the flux measured in the tenth XRT observation, as this data point had both a constrained X-ray and UVOT measured flux. In Figure 8 (middle panel) we plot the solar wind proton flux, at the three observing periods as described below. The lower panel of Figure 8 shows  $N_{\text{gas}}$  over the periods of the observations.

There are several competing processes that contribute to the predicted X-ray flux as given in Equation 2. The gas production rate was 50% larger in January compared to the other observing periods, however the comet was at half the distance from Earth in February and March. The average proton flux was comparable during 2009-01-28 and 2009-03-04, and about 40% lower during our 2009-02-16 observations. The contributing parameters to the predicted lightcurve compete to cancel each other out, resulting in a relatively flat predicted X-ray lightcurve. Thus our measurements do not exhibit any large variations, and our predicted and measured lightcurves are in reasonably good agreement.

The solar proton flux is only a proxy for the heavy ion flux of the solar wind and this heavy ion content may vary considerably due to variations in either solar wind atomic abundance or ion temperature and charge state. Thus we looked at additional available solar wind  $\text{O}^{7+}$  flux data during the time of our observations (e.g. from the Advanced Composition Explorer (ACE), Stone et al. 1998), located at Lagrangian Point L1). Unfortunately the available data were sparse and of low quality.

Had the comet interacted with a ICME (a large cloud of plasma ejected from the Sun, as described in Section 1) during our observations, we would have in general expected a large increase in the measured X-ray flux and spectral hardness due to the presence of highly charged ions (as shown by the examples of an ICME interacting with the exosphere of the Earth; Ezoe et al. 2011; Carter et al. 2010). Approximately 10% of ICMEs appear to exhibit only weak compositional anomalies (Richardson & Cane 2004). The long-term trend data of Figure 7 suggested that during at least one, if not two of the observing periods, the comet had sampled a CIR. CIRs occur when a fast solar wind stream piles up against a slow solar wind

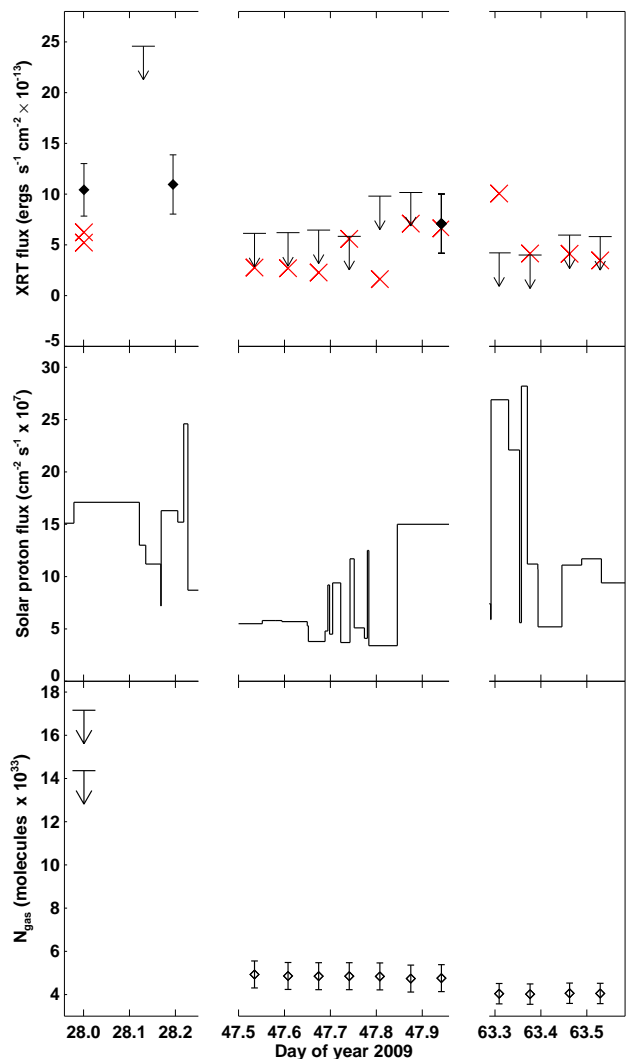


**Fig. 8.** Upper panel: XRT 0.3 to 1 keV background-corrected fluxes (diamonds) or upper limits (downward arrows) where appropriate, plotted against a time-axis given in the day of year. We also plot the predicted X-ray flux (red crosses, normalised to the tenth observation) as described in the text. Middle panel: solar wind proton flux as measured by STEREO A for early 2009. Lower panel:  $N_{\text{gas}}$  (open diamonds), or upper limits (downward arrows) where appropriate.

stream. CIRs show average compositional signatures similar to average fast and cool solar wind (Mason et al. 2008). Hence, the comet may have sampled, or partially sampled, a fast, cool plasma that would have exhibited lower abundances of highly-charged heavy ions that are responsible for X-ray emitting, charge-exchange interactions. The X-ray spectrum of Lulin is indicative of a higher solar wind charge state than the very soft X-ray spectrum of comet 17P/Holmes (Christian et al. 2010), which showed no X-ray emission above 0.4 keV and was postulated to be the result of an interaction with the cool, polar solar wind.

#### 4. Conclusions

We have used the unique capabilities of the *Swift* observatory to simultaneously observe comet C/2007 N3 (Lulin) via UV and X-ray emission. We have carefully transformed X-ray events from 14 *Swift* XRT pointings towards comet Lulin to produce the optimum exposure-corrected X-ray image. We have also analysed *Swift* UVOT exposures when available and used this data to observe variations in the morphology of the comet in particular with regards to the dust and ion tails. We see the peak of the cometary X-ray emission offset from the peak in the UV emission, and this offset is displaced towards the Sun, indicating that the coma was collisionally thick to charge exchange from the nucleus out to about 35,000 km, as expected for a comet with a gas production rate of  $Q_{\text{H}_2\text{O}} = 6 \times 10^{28} \text{ mol. s}^{-1}$ .

A model applied to a background-corrected X-ray spectrum was consistent with emission from charge exchange, although individual lines were heavily blended. The spectrum, only discernible below 1 keV, also suggested that the comet had sampled a cool solar wind, with less highly ionised oxygen than a quiescent (warm) equatorial solar wind. Such a spectrum may be expected if the comet had encountered a stream of fast wind originating at the cold base of the corona and flowing through a coronal hole. We have used the solar wind proton flux as a proxy for solar wind activity throughout this work, as investigations regarding solar wind minor ion fluxes were hampered by a lack of high cadence data from spacecraft solar wind ion monitors during the *Swift* observations. What heavy ion data trends that do exist suggest there were indeed numerous CIRs during the period of the *Swift* Lulin observations.

We combined our simultaneous X-ray and UV observations with measured solar wind data to explain the measured X-ray lightcurve. We use data from the *Swift* UVOT, employing the uvw1 and v-band filters to measure the number of OH molecules in the FOV and estimate the number of water molecules released by the comet. We used the water production rates of the comet and solar wind data mapped to the location of the comet to estimate the expected X-ray flux. We demonstrate that Lulin's X-ray brightness was determined by the comet's activity and the observing geometry, as well as variations in the solar wind.

*Acknowledgements.* The authors would like to thank the *Swift* instrument teams for all their help and advice, and T. L. Farnham (University of Maryland) for a most helpful discussion on the observing geometry and for running his synchrone/syndine calculation for these observations. The authors also thank S. Lepri (University of Michigan) for the interpretation of the space weather data. J. A. Carter and A. M. Read gratefully acknowledge funding by the Science and Technology Facilities Council, U.K. We thank the anonymous referee for the suggestions for improvement which have greatly enhanced the manuscript.

#### References

- Beiersdorfer, P., Boyce, K. R., Brown, G. V., et al. 2003, *Science*, 300, 1558
- Blush, L. M., Allegrini, F., Bochslers, P., et al. 2005, *Advances in Space Research*, 36, 1544
- Bodewits, D., Christian, D. J., Torney, M., et al. 2007, *A&A*, 469, 1183
- Bodewits, D., Lisse, C., Christian, D. J., et al. 2006, in *Bulletin of the American Astronomical Society*, Vol. 38, AAS/Division for Planetary Sciences Meeting Abstracts #38, 533
- Bodewits, D., Villanueva, G. L., Mumma, M. J., et al. 2011, *AJ*, 141, 12
- Bonev, B., Gibb, E., Villanueva, G., et al. 2009, in *AAS/Division for Planetary Sciences Meeting Abstracts*, Vol. 41, AAS/Division for Planetary Sciences Meeting Abstracts 41, 23.07–+
- Breeveld, A. A., Landsman, W., Holland, S. T., et al. 2011, *ArXiv e-prints*
- Burrows, D. N., Hill, J. E., Nousek, J. A., et al. 2005, *Space Science Reviews*, 120, 165
- Carter, J. A., Sembay, S., & Read, A. M. 2010, *MNRAS*, 402, 867
- Cash, W. 1979, *ApJ*, 228, 939
- Christian, D. J., Bodewits, D., Lisse, C. M., et al. 2010, *ApJS*, 187, 447
- Collier, M. R., Moore, T. E., Snowden, S. L., & Kuntz, K. D. 2005, *Advances in Space Research*, 35, 2157
- Combi, M. R., Bertaux, J.-L., Quemerais, E., & Maekinen, J. T. T. 2009, *IAU Circ.*, 9020, 1
- Combi, M. R., Harris, W. M., & Smyth, W. H. 2004, *Gas dynamics and kinetics in the cometary coma: theory and observations*, ed. Festou, M. C., Keller, H. U., & Weaver, H. A., 523–552
- Cravens, T. E. 1997, *Geophys. Res. Lett.*, 24, 105
- Dennerl, K., Aschenbach, B., Burwitz, V., et al. 2003, in *Society of Photo-Optical Instrumentation Engineers (SPIE) Conference Series*, Vol. 4851, Society of Photo-Optical Instrumentation Engineers (SPIE) Conference Series, ed. J. E. Truemper & H. D. Tananbaum, 277–288
- Dennerl, K., Englhauser, J., & Trümper, J. 1997, *Science*, 277, 1625
- Ezoe, Y., Miyoshi, Y., Yoshitake, H., et al. 2011, *ArXiv e-prints*
- Feldman, U., Landi, E., & Schwadron, N. A. 2005, *Journal of Geophysical Research (Space Physics)*, 110, 7109
- Festou, M. C. 1981, *A&A*, 95, 69
- Gehrels, N., Chincarini, G., Giommi, P., et al. 2004, *ApJ*, 611, 1005
- Geiss, J., Gloeckler, G., von Steiger, R., et al. 1995, *Science*, 268, 1033
- Godet, O., Beardmore, A. P., Abbey, A. F., et al. 2009, *A&A*, 494, 775
- Gosling, J. T. & Pizzo, V. J. 1999, *Space Sci. Rev.*, 89, 21
- Haser, L. 1957, *Bulletin de la Societe Royale des Sciences de Liege*, 43, 740
- Huebner, W. F., Keady, J. J., & Lyon, S. P. 1992, *Ap&SS*, 195, 1
- Kharchenko, V. & Dalgarno, A. 2001, *ApJ*, 554, L99
- Kharchenko, V., Rigazio, M., Dalgarno, A., & Krasnopolsky, V. A. 2003, *ApJ*, 585, L73
- Knight, M. & Schleicher, D. 2009, *IAU Circ.*, 9025, 1
- Koutroumpa, D., Lallement, R., Kharchenko, V., et al. 2006, *A&A*, 460, 289

- Krasnopolsky, V. 1997, *Icarus*, 128, 368
- Krasnopolsky, V. A. 2006, *Journal of Geophysical Research (Space Physics)*, 111, A12102
- Lin, Z. Y., Weiler, M., Rauer, H., & Ip, W. H. 2007, *A&A*, 469, 771
- Lisse, C. M., Christian, D., Dennerl, K., et al. 1999, *Icarus*, 141, 316
- Lisse, C. M., Christian, D. J., Dennerl, K., et al. 2001, *Science*, 292, 1343
- Lisse, C. M., Christian, D. J., Dennerl, K., et al. 2005, *ApJ*, 635, 1329
- Lisse, C. M., Cravens, T. E., & Dennerl, K. 2004, X-ray and extreme ultraviolet emission from comets, ed. Festou, M. C., Keller, H. U., & Weaver, H. A., 631–643
- Lisse, C. M., Dennerl, K., Christian, D. J., et al. 2007, *Icarus*, 191, 295
- Lisse, C. M., Dennerl, K., Englhauser, J., et al. 1996, *Science*, 274, 205
- Mason, G. M., Leske, R. A., Desai, M. I., et al. 2008, *ApJ*, 678, 1458
- Mason, K. O., Breeveld, A., Hunsberger, S. D., et al. 2004, in Presented at the Society of Photo-Optical Instrumentation Engineers (SPIE) Conference, Vol. 5165, Society of Photo-Optical Instrumentation Engineers (SPIE) Conference Series, ed. K. A. Flanagan & O. H. W. Siegmund, 277–286
- Mawhorter, R. J., Chutjian, A., Cravens, T. E., et al. 2007, *Phys. Rev. A*, 75, 032704
- Neugebauer, M., Cravens, T. E., Lisse, C. M., et al. 2000, *J. Geophys. Res.*, 105, 20949
- Ootsubo, T., Usui, F., Kawakita, H., et al. 2010, *ApJ*, 717, L66
- Pagani, C., Beardmore, A. P., Abbey, A. F., et al. 2011, *A&A*, 534, A20+
- Parker, E. N. 1958, *ApJ*, 128, 664
- Poole, T. S., Breeveld, A. A., Page, M. J., et al. 2008, *MNRAS*, 383, 627
- Richardson, I. G. & Cane, H. V. 2004, *Journal of Geophysical Research (Space Physics)*, 109, 9104
- Roming, P. W. A., Kennedy, T. E., Mason, K. O., et al. 2005, *Space Sci. Rev.*, 120, 95
- Schleicher, D. G. & A'Hearn, M. F. 1988, *ApJ*, 331, 1058
- Schleicher, D. G. & Farnham, T. L. 2004, Photometry and imaging of the coma with narrowband filters, ed. Festou, M. C., Keller, H. U., & Weaver, H. A., 449–469
- Schwadron, N. A. & Cravens, T. E. 2000, *ApJ*, 544, 558
- Shi, J. C., Lin, Q. S., Hu, Z. W., Zhao, H. B., & Ma, Y. H. 2011, *Acta Astronomica Sinica*, 52, 136
- Snowden, S. L., Freyberg, M. J., Plucinsky, P. P., et al. 1995, *ApJ*, 454, 643
- Stone, E. C., Frandsen, A. M., Mewaldt, R. A., et al. 1998, *Space Science Reviews*, 86, 1
- Wegmann, R. & Dennerl, K. 2005, *A&A*, 430, L33
- Wegmann, R., Dennerl, K., & Lisse, C. M. 2004, *A&A*, 428, 647
- Willingale, R., O'Brien, P. T., Cowley, S. W. H., et al. 2006, *ApJ*, 649, 541
- Wolk, S. J., Lisse, C. M., Bodewits, D., Christian, D. J., & Dennerl, K. 2009, *ApJ*, 694, 1293
- Zhao, L., Zurbuchen, T., & Fisk, L. 2007, AGU Fall Meeting Abstracts, A276
- Zurbuchen, T. H. & Richardson, I. G. 2006, *Space Science Reviews*, 123, 31